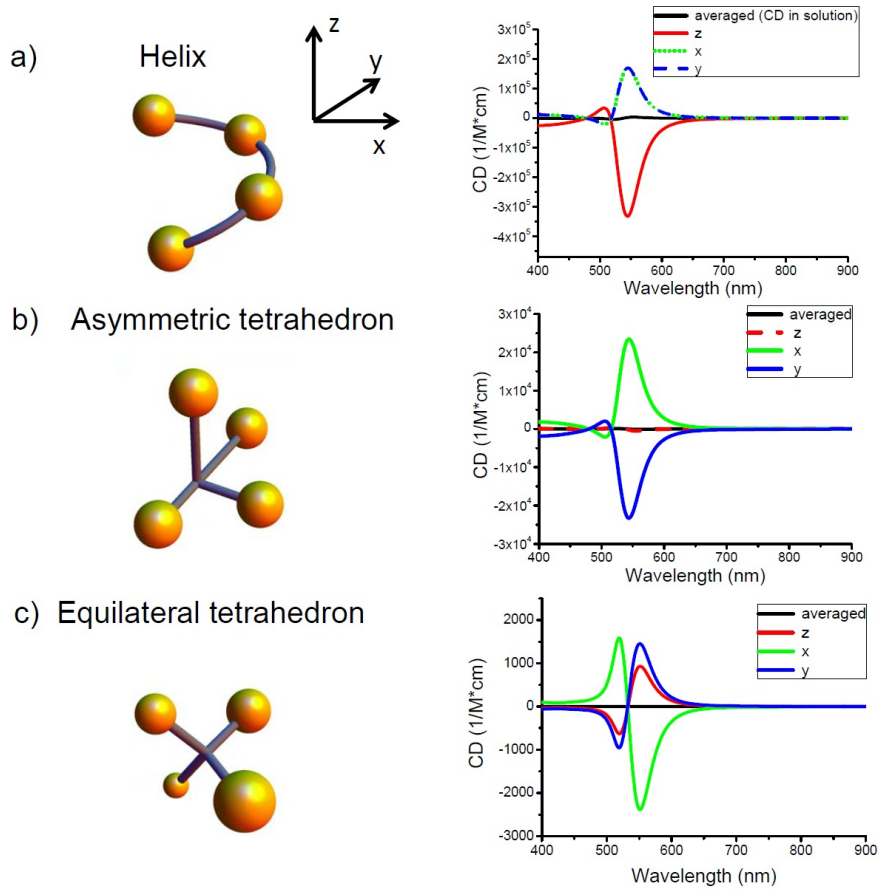

Supplementary Figure S1 | Calculated CD spectra for three chiral assemblies shown on the left-hand side of the figure. The averaged CD describes the signals coming from a solution; the directional CD spectra are shown for three representative directions, +x, +y, +z. Parameters of the assemblies are given below, in **Supplementary Table S1**. It is interesting to compare CD of a plasmonic helix with CD signals of other geometries, such as tetrahedral complexes for example[37-39]. Three chiral geometries of a plasmonic tetramer are shown. We can see that the helical assembly has a clear advantage over the other geometries with tetrahedral arrangements. In a helix, the CD signals are one/two orders of magnitude higher than the CD signals in asymmetric and equilateral tetrahedral complexes. The data was taken from Ref. 38. A chiral plasmonic assembly with an equilateral tetrahedral frame **(c)** has the smallest CD signals. In fact, the averaged CD for this assembly has a vanishing magnitude for the given geometrical parameters. The reason is that such a tetrahedral assembly has no dipolar CD in solution and may have non-vanishing CD signals only due to the multipole interactions between nanoparticles. Simultaneously, a

helical assembly **(a)** has a very strong dipolar CD. The shapes of CD signals for assemblies of various geometries are typically similar. The reason lies in the physics of the CD signal formation: the CD signal appears due to the Coulomb and electromagnetic interactions between plasmons of single nanoparticles, and these interactions lead to the formation of collective plasmon modes with chiral properties. In an assembly, the integral of the CD spectrum over the frequency should be approximately zero due to the optical sum rule and, therefore, the shape of CD is typically bi-signate (dip-peak or peak-dip). The collective plasmonic spectrum of a chiral assembly has right-handed and left-handed plasmonic excitations on the two opposite sides of the plasmon peak; therefore, this property produces characteristic bi-signate lines in the CD spectra. The data for directional CD is also shown. Again we see that the helical assembly **(a)** demonstrates the strongest signals. Another general property of the plasmonic CD signals can be seen in this figure: the directional CD signals are typically much stronger than the averaged CD in solution.

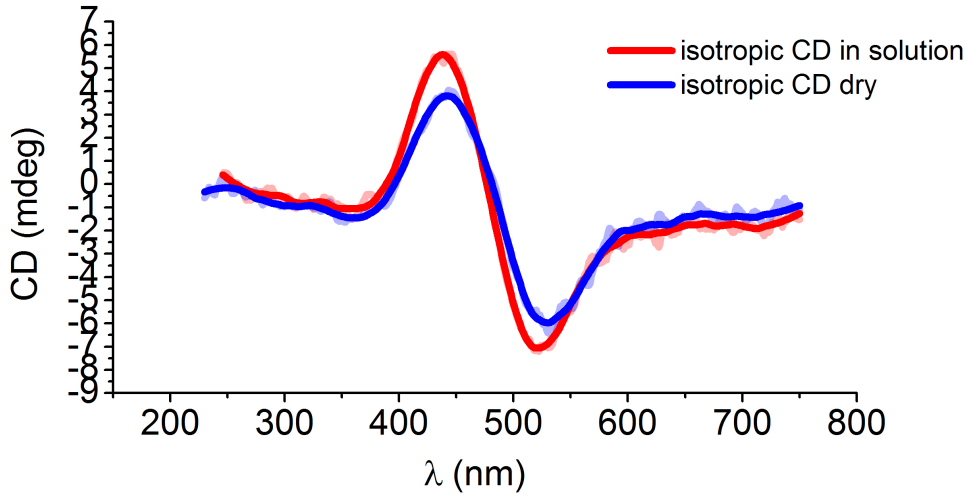

Supplementary Figure S2 | CD spectra of left-handed nanohelices randomly orientated in solution and on a substrate. These measurements were performed with the same ensemble of left-handed nanohelices, which were isotropically distributed in solution (red curve) and were then simply left to dry on a glass surface (blue curve). In contrast to the other experiments, the structures were not attached to the surface via biotin linkers. Also, no washing step was used to flush away unbound structures. Here, enough material was used to enable the formation of a thin film of dried, but randomly oriented helices. An influence of the change of the refractive index may be observed as a 4 nm shift of the peak and a 10 nm shift of the dip of the CD signal. It is also possible that the helices are not distributed completely isotropically but have a tendency to align parallel to the surface. This effect must be, however, negligible as no significant change in the shape of the CD signal is observed.

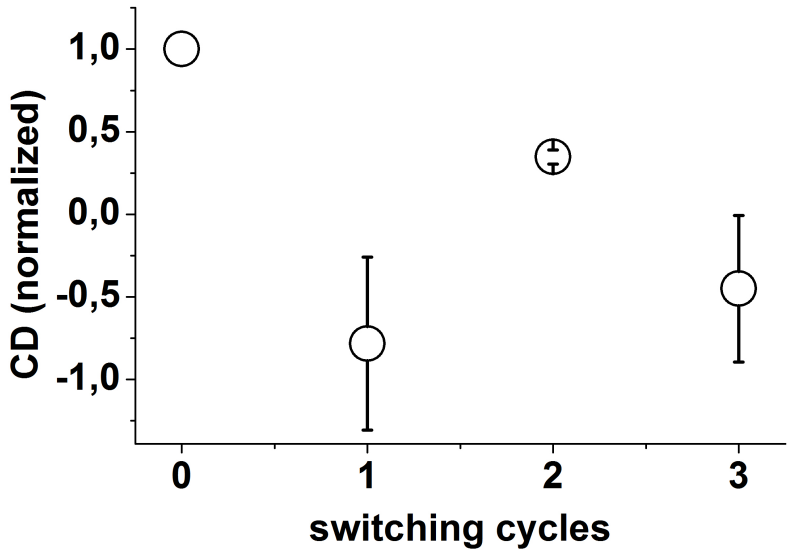

Supplementary Figure S3 | Progression of the CD signal of L-NHs with switching cycles averaged over 4 experiments. Each data point represents the averaged and normalized maximum peak or dip value of the CD signals of 4 different experiments going through up to 4 switching states. We attribute the decrease of the maximum signals over switching cycle to the following scenarios: at each drying step, some of the nanohelices get trapped in a specific orientation on the surface (most likely lying on the surface) and at each washing step some of the helices (but also individual gold particles) detach from the surface. Any other form of helix destruction or deformation will lead to a loss of signal or the helices.

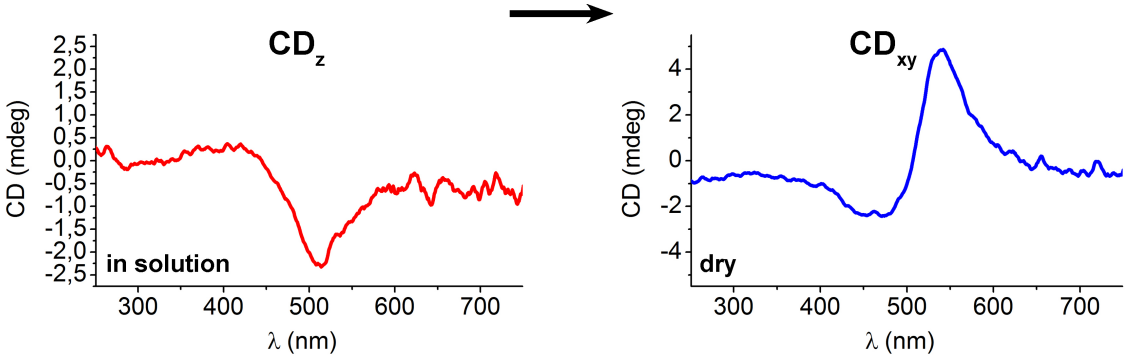

Supplementary Figure S4 | Switching of R-NH with inverted CD signals. This experiment was performed as described for L-NH in the main text. The recorded CD signal clearly shows the expected switching behavior. Right-handed nanohelices that are upright in solution (left) show a CD_Z signal that is inverted to the CD_Z signal of L-NHs. After being switched by drying to an orientation parallel to the surface the CD_{xy} signal that is inverted to the CD_{xy} signal of lying L-NHs is recorded.

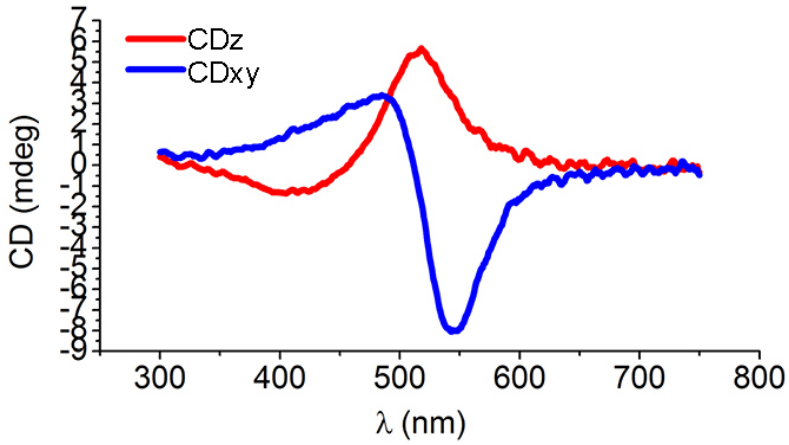

Supplementary Figure S5 | Switching CD spectra of L-NHs prepared by directly conjugating gold nanoparticles to 24HB attached to the surface. Measurements were performed with the same ensemble of left-handed nanohelices in solution (red curve) and dried (blue curve).

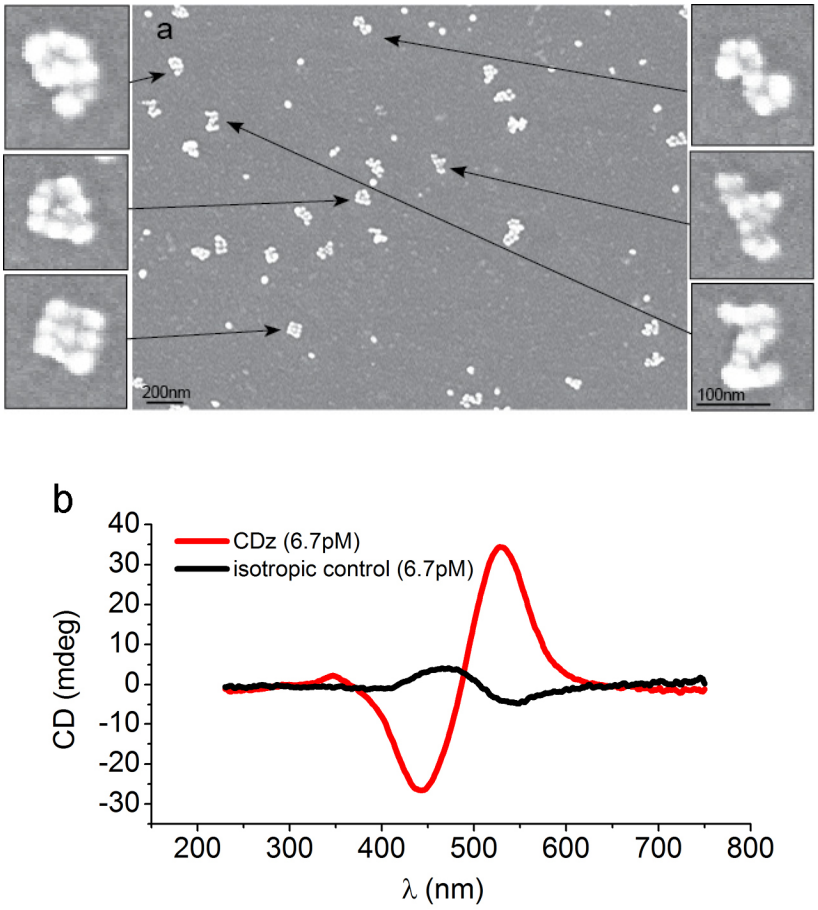

Supplementary Figure S6 | CD comparison of oriented and randomly distributed helices (a) Wide field Scanning Electron Microscopy (SEM) image of left-handed Nanohelices attached to a BSA-biotin-neutravidin coated quartz surface. An area density of five left-handed nanohelices per μm^2 was determined. Zoom-in images reveal that super-enhanced helices remain partly upright even after drying. (**b**) A CD of 35 mdeg for anisotropic left-handed nanohelices was measured at an area density of five nanohelices per μm^2 (silver enhanced attached helices in buffer, red curve). Silver enhanced helices dispersed in solution at the same area density (area density was converted to volume concentration by mapping the projection of the three-dimensional volume to a two-dimensional plane) result in a CD peak maximum of 4.5 mdeg (black curve). Hence the anisotropic CD is roughly one order of magnitude (~8 times) higher than the isotropic CD of the L-NHs. The shape of the anisotropic CD_z signal presented here differs slightly from the previous presented CD_z spectra (Figures 1 and 2, main text). Such variations may result from different silver enhancement conditions in each set of experiments. Here, a stronger silver enhancement was necessary to enable imaging of the nanohelices with SEM.

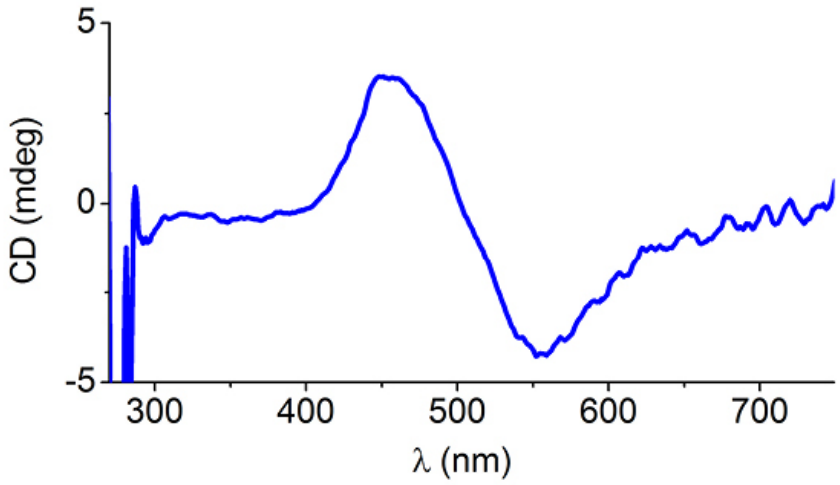

Supplementary Figure S7 | L-NHs on an amine-silane coated glass slide in solution. Assembled nanohelices were deposited on an amine-silane coated glass in 0.5xTBE buffer (pH 6, 11 mM $MgCl_2$) for 2 hrs. The recorded CD signal of this sample is switched compared to the signal from nanohelices standing in solution and differs slightly from dried helices (see e.g. Figure 1, main text). This is in accordance with our expectation as we expect the charge-induced adsorption (DNA is strongly negatively charged) to predominantly result in helices aligned parallel to the surface, but some helices may also attach upright to the surface as the structures has an aspect ration of only ~ 5:1.

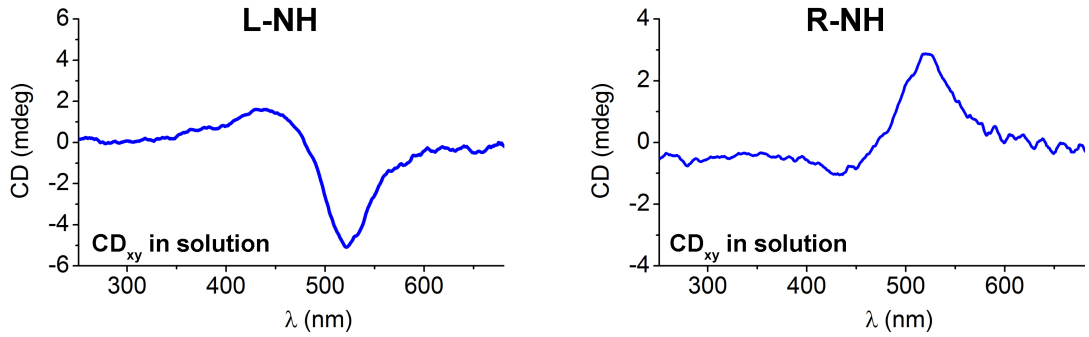

Supplementary Figure S8 | Solution measurement of L- and R-NHs attached parallel to the substrate. A BSA-Neutravidin surface was prepared as describe in the methods section of the main text. Instead of biotinylated nanohelices this time biotynilated poly-A-oligonucleotides (15 bases) were applied to the surface. After washing, nanohelices without biotin were added. As all nine gold nanoparticles of the nanohelices are densely covered with poly-T-oligonucleotides, the helices were tightly coupled via doublestrand formation to the substrate in a parallel fashion. As expected, we recorded clear CD signals of the xy-modes for these samples.

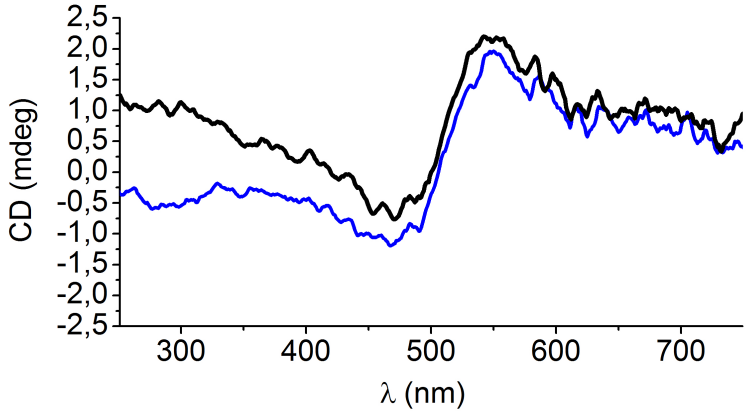

Supplementary Figure S9 | CD signal artifacts by a 90° rotation of the substrate. R-NHs were aligned parallel to the quartz substrate by an airstream. The first spectra (blue) was taken at a given orientation of the substrate in the cuvette (surface pependicular to the probing beam). For the second experiment the substrate was rotated 90° around its normal. As a result we observe a distinct chance of the CD signal in the UV and the blue region of the spectrum.

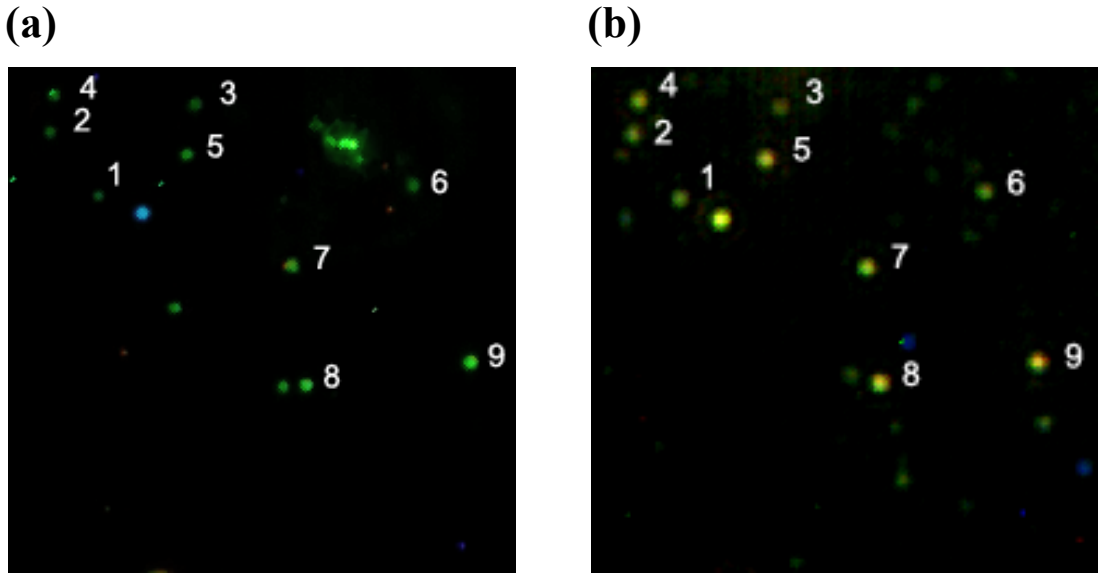

Supplementary Figure S10 | Darkfield colour image of surface-bound nanohelices in solution (a) and after they are dried (b). The nanohelices with a number placed next to it were measured spectroscopically (data shown in **Supplementary Figure S11**). The colour change between the two images indicates that the scattering spectra is red shifted, consistent with the change of nanohelices' orientation from up-right in solution to lying-flat in the dry condition. The out-of-focus object in **(a)** is most likely an unbound nanostructure floating in solution.

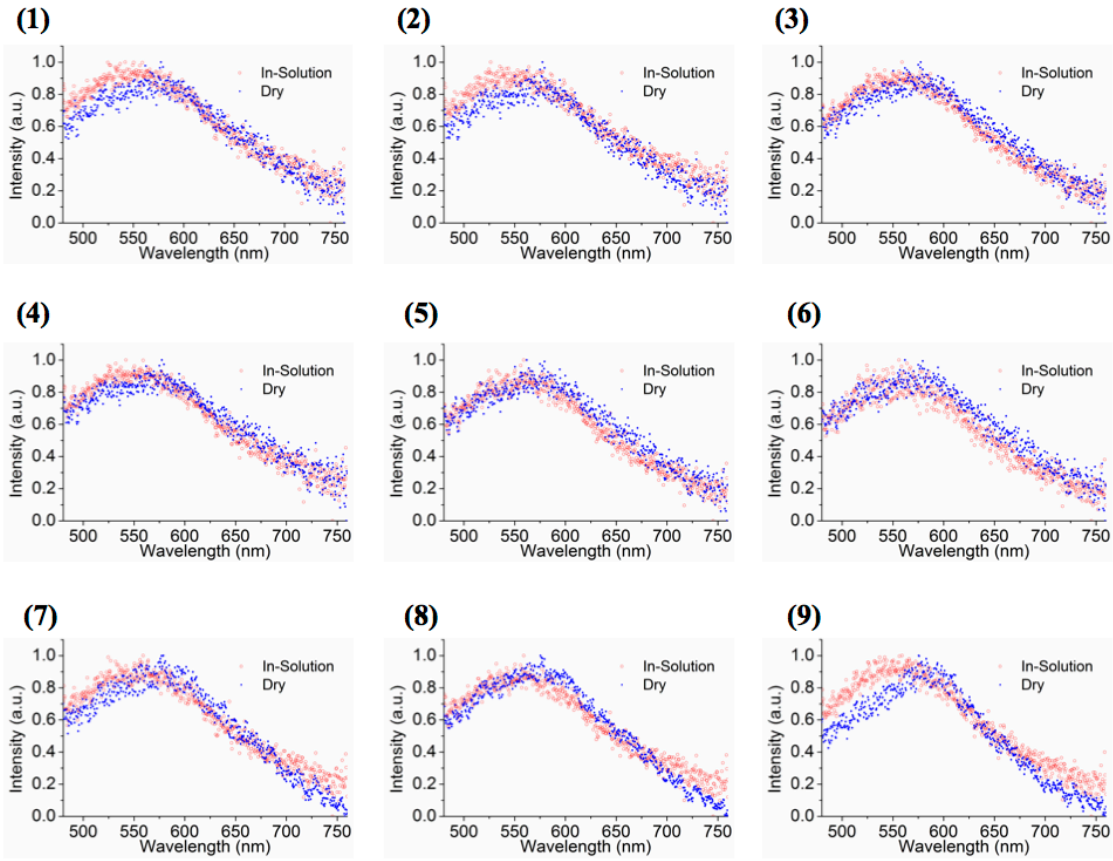

Supplementary Figure S11 | Darkfield colour scattering spectra of 9 surface-bound nanohelices (as labelled in Supplementary Figure S10). Each plot consists of a scattering spectrum of a nanohelix in solution and of a spectrum of the same nanohelix after it was dried. The peak scattering wavelength shows a red shift after the nanohelices were dried. The sub-captions for each figure correspond to the numerical labels shown in **Supplementary Figure S10**. Some variations in the scattering spectra among different nanohelices are observed. In general, the peak scattering wavelength for nanohelices in solution is at 554 ± 8 nm and the peak scattering wavelength for nanohelices after they are dried is at 576 ± 10 nm.

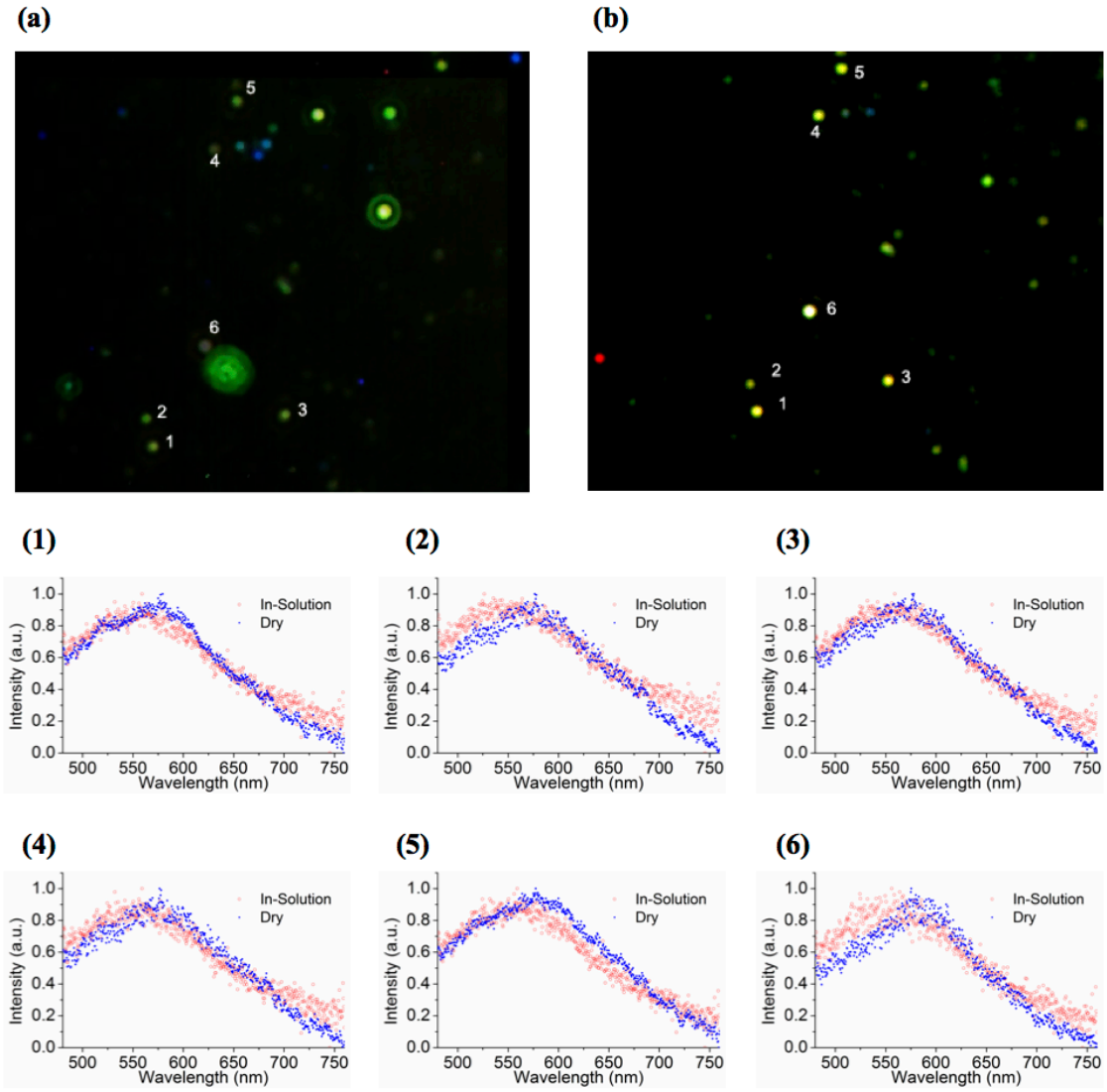

Supplementary Figure S12 | Darkfield image of surface-bound nanohelices in solution (a) and after they are dried (b). (1)-(6) Darkfield scattering spectra of the nanohelices labelled in **(a)** and **(b)**. It can be observed that the scattering spectra are not polarization dependent for nanohelices in solution. However, the scattering spectra show a considerable polarization dependency after the nanohelices are dried.

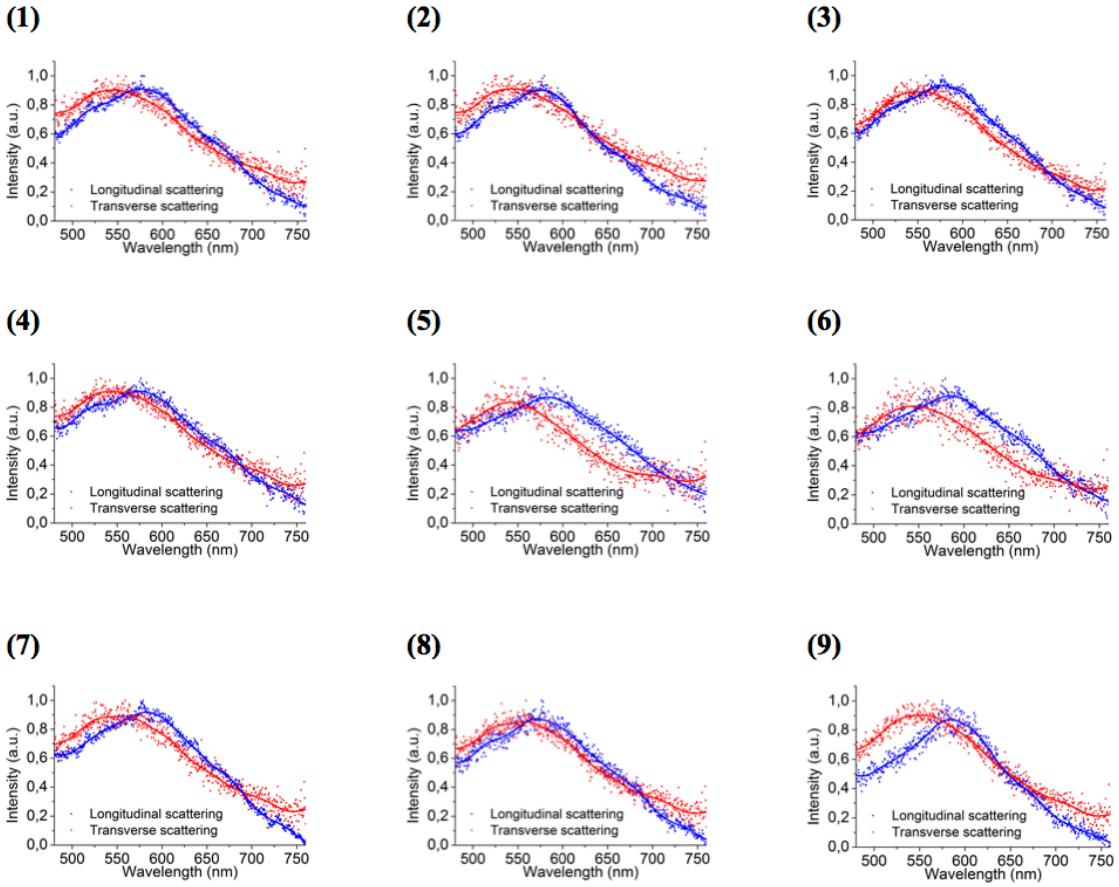

Supplementary Figure S13 | Longitudinal and transverse darkfield scattering spectra for dry, surface-bound nanohelices shown in Supplementary Figure S10. Additional scattering spectra of bound nanohelices for longitudinal and transverse polarizations. During the measurements, a linear polarizer is rotated until a maximum total scattering intensity is observed. The darkfield scattering spectrum for this polarizer angle is considered as the longitudinal scattering. The polarizer is then rotated by 90° to obtain the darkfield spectrum for the transverse scattering.

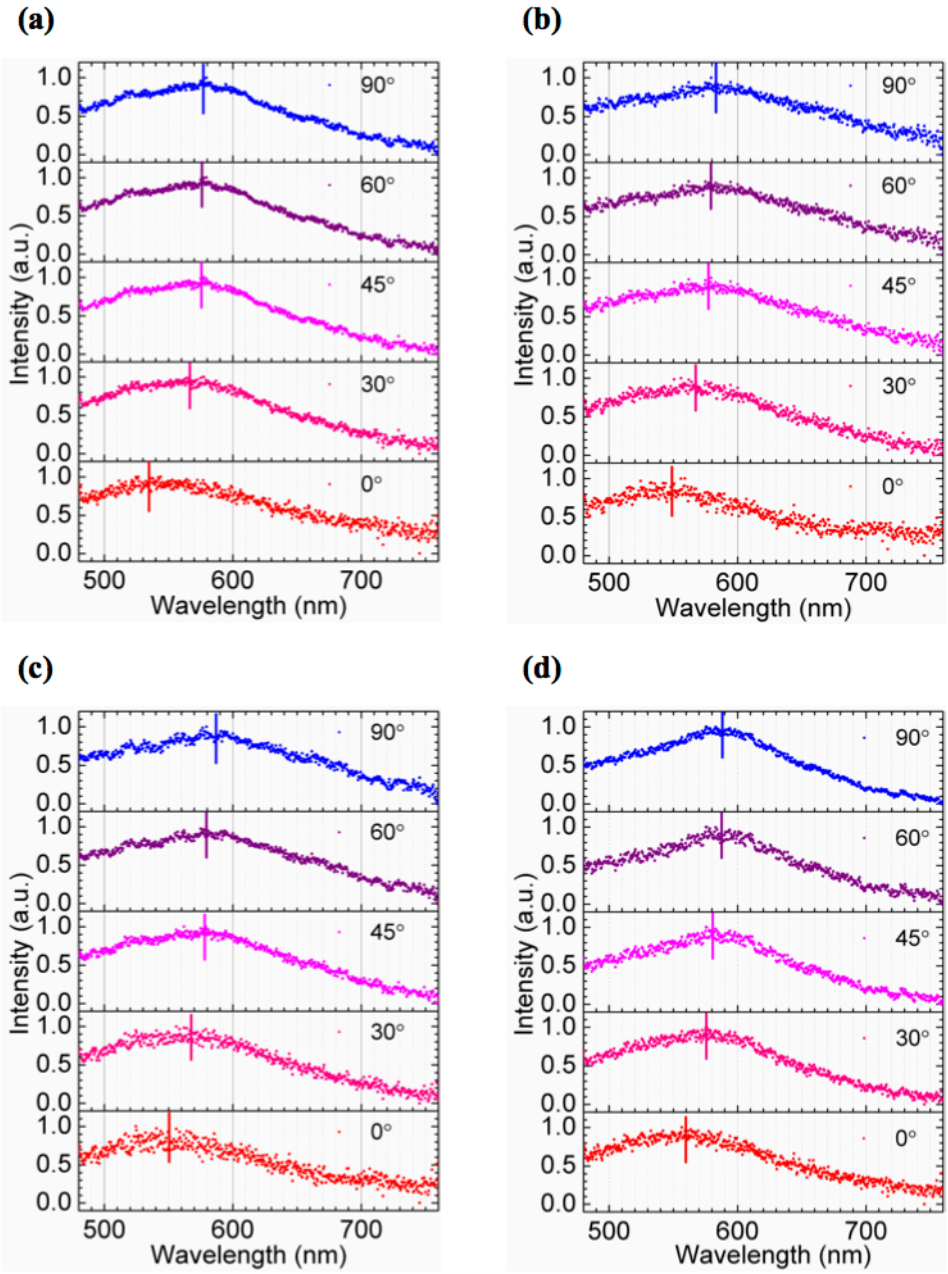

Supplementary Figure S14 | Polarization dependency of darkfield scattering spectra for a surface-bound nanohelix dried on glass. The scattering spectra as a function of linear polarizer orientation were measured. Typical data is shown here. The angle of the linear polarizer is 0º for the transverse scattering and 90º for the longitudinal scattering, respectively.

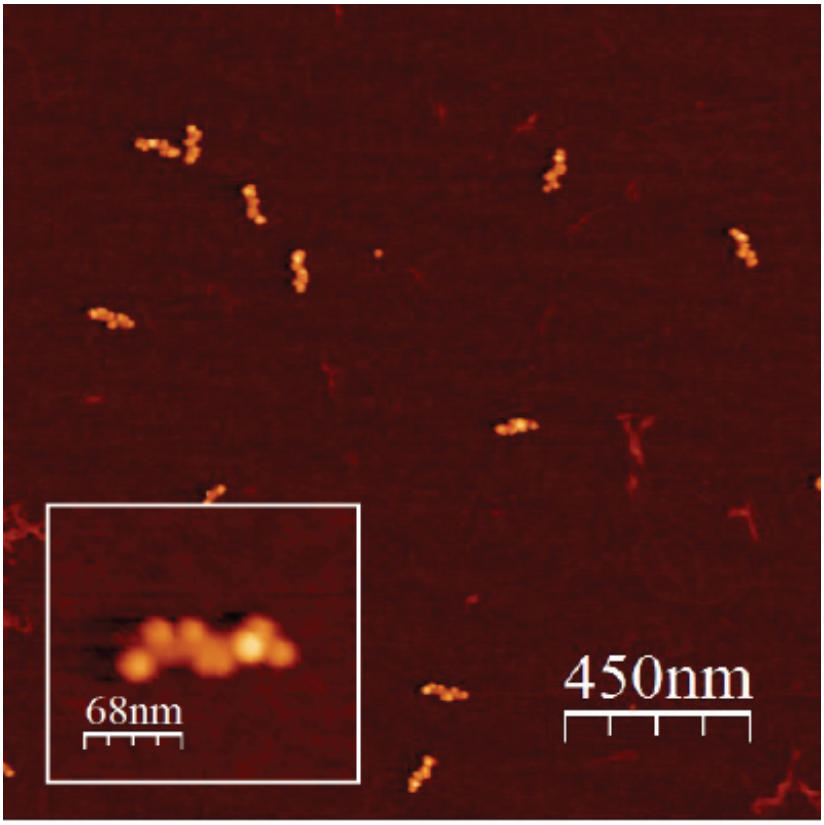

Supplementary Figure S15 | AFM image of dried L-NH on a quartz surface.

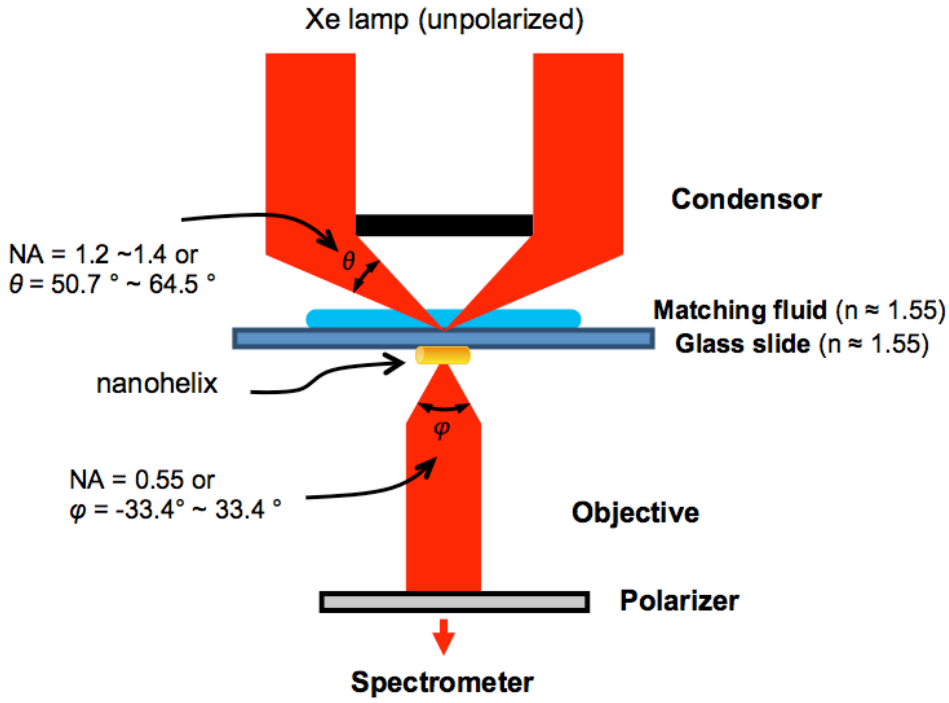

Supplementary Figure S16 | Schematic drawing of the optical setup used to characterize the nanohelices. The glass slide is illuminated by an unpolarised Xe lamp through a high NA condenser (Cytoviva). The light scattered by an individual nanohelix is collected by a 100x objective lens using an adjustable NA of 0.55. The light is fed to a CCD spectrometer (Acton 300i, Princeton Instrument) either directly or via an adjustable linear polarizer.

Coordinates and Radii (nm)	*x*	*y*	*z*	radius
Helix	14.376	0	0	5
	0	14.376	8.386	5
	-14.376	0	16.772	5
	0	-14.376	25.158	5
Asymmetric Tetrahedron	15.56	0	0	5
	0	23.34	0	5
	0	-15.56	0	5
	0	0	23.34	5
Equilateral Tetrahedron	8.4852	8.4852	8.4852	3
	-8.4852	-8.4852	8.4852	4
	8.4852	-8.4852	-8.4852	5
	-8.4852	8.4852	-8.4852	6

Supplementary Table S1. Coordinates and radii of nanoparticles in the chiral assemblies.

Supplementary Note 1: Dipolar model of nanoparticle helix

Calculations in the manuscript follow the electrodynamics methods used previously in Refs. 37-41. A system of nanoparticles (NPs) is described by a set of dipoles $\vec{p}_i$ induced by the electric fields. The NPs are arranged in a helix (Figures 1 and 3 in the main text). The equation for a dipole of a single NP with index i is

$$\vec{p}_i = \alpha\left(\vec{E}_{ext,i} + \sum_{j\neq i}\vec{E}_{j\to i}\right), \qquad \textbf{(S1)}$$

where $\vec{E}_{ext,i}$ is the external field, α is the polarizability of a NP, and $\vec{E}_{j\to i}$ is the field due to the neighboring NPs:

$$\vec{E}_{j\to i} = \left\{\left(1-\frac{i\omega\sqrt{\varepsilon_0}r_{ji}}{c}\right)\frac{3\hat{r}_{ji}\cdot\vec{p}_j\hat{r}_{ji}-\vec{p}_j}{r_{ji}^{\,3}} + \varepsilon_0\frac{\omega^2}{c^2}\frac{\vec{p}_j-\hat{r}_{ji}\cdot\vec{p}_j\hat{r}_{ji}}{r_{ji}}\right\}e^{\frac{i\omega\sqrt{\varepsilon_0}r_{ji}}{c}}. \qquad \textbf{(S2)}$$

The NP polarizability is defined in the usual way: $\alpha(\omega) = R_{NP}^3\left(\varepsilon_{Au}-\varepsilon_0\right)/\left(\varepsilon_{Au}+2\varepsilon_0\right)$, where R_{NP} is the NP radius, $\varepsilon_{Au}(\omega)$ is the Au dielectric function, and ε_0 is the dielectric constant of matrix. The external field varies at different sites by a phase factor $e^{i\vec{k}\cdot\vec{r}_i}$. The set of linear equations (1) can be solved self-consistently for all dipole moments. Then, the total absorption and extinction rates can be calculated using the following equations:

$$(Q_{abs} = \frac{1}{2}\omega\cdot\varepsilon_0\sum_i \mathrm{Im}\left(\frac{\vec{p}_i^{\,*}}{\alpha^*}\cdot\vec{p}_i\right), \qquad \textbf{(S3)}$$

$$Q_{ext} = \frac{1}{2}\omega\cdot\varepsilon_0\sum_i \mathrm{Im}\left(\vec{E}_{ext\_i}^{\,*}\cdot\vec{p}_i\right). \qquad \textbf{(S4)}$$

The scattering rate is calculated: $Q_{scat} = Q_{ext} - Q_{abs}$.

The directional CD for incident light associated with a particular wave vector $\vec{k}$ is given by

$$CD_{\vec{k}} = Q_{ext,+} - Q_{ext,-}, \qquad \textbf{(S5)}$$

where the symbols ± are related to the LCP and RCP photons. In colloidal solution systems, the nanostructures are randomly oriented and we need to perform averaging over orientations. Mathematically, averaging can be performed by assuming that the light comes from all directions to a nanostructure with a fixed orientation:

$$\langle CD \rangle = \langle Q_+ - Q_- \rangle_{\Omega_k^r}. \qquad \textbf{(S6)}$$

The calculations of CD and scattering in the main text are based on Eqs. S3-S6. In Fig. 3d in the main text, we show the data for CD averaged over an interval of the angle of tilting,

$$CD(\theta) = \frac{\int_0^{\theta} CD_{k\|-\hat{z}}^{r}(\theta') \cdot \sin[\theta'] d\theta'}{\int_0^{\theta} \sin[\theta'] d\theta'}, \qquad \textbf{(S7)}$$

where θ is the angle giving the tilting of the helix with respect to the normal (see Fig. 3d in the main text). For the medium, we assumed water ($\varepsilon = 1.8$) and for Au dielectric function we used the tables from Ref. 42.